CHAPTER- I

Introduction and Literature Review

1.1 Introduction

Study of magnetoelectric multiferroics, in which the antiferromagnetic (AFM) or ferromagnetic (FM) and antiferroelectric (AFE) or ferroelectric (FE) orders coexist and are mutually coupled, is a hot topic in materials science [Ramesh and Spaldin (2007); Eerenstein et al. (2006); Hill (2000); Khomskii et al. (2006); Tokura et al. (2006); Kimura (2003)]. The coexistence and coupling of the magnetic (M) and electric order parameters (P) in a single phase multiferroic material leads to novel physical phenomena and offers possibilities for new multifunctional sensors, actuators, data storage devices and 4-state logic systems [Fiebig (2005); Khomskii (2006); Scott (2007); Wang et al. (2009)]. Among these interesting materials, $BiFeO_3$ has attracted intense research interest because it is only room temperature multiferroic till exists [Wang et al. (2003); Fiebig (2005)]. The present thesis deals with the structural and ferroic properties of $BiFeO_3$-$xPb(Fe_{0.5}Nb_{0.5})O_3$ (BF-xPFN) solid solution system. This chapter includes the general introduction about ferroelectricity and magnetism along with discussion on different types of the magnetic exchange-interaction phenomenon. Further, it is followed by the brief review of literature on different mechanisms of coexistence of ferroelectric and magnetic order also. The literature review on BF-xPFN solid solution is presented at the end of this chapter.

1.2 General description of the perovskite structure

Any material with the same type of the crystal structure as the calcium titanate ($CaTiO_3$), is known as the perovskite structure. Perovskites take their

name from this compound, which was first discovered by Gustav Rose in 1839 and is named after Russian mineralogist, L. A. Perovski [1792-1856]. The general chemical formula for an ideal perovskite compound is ABO_3, where 'A' and 'B' are two cations and 'O' is an anion. In the perovskite structure the B cation has a 6-fold coordination i.e. octahedral coordination and A cation has 12-fold cuboctahedral coordination. The ideal perovskite structure belongs to the cubic crystal system in the $Pm\bar{3}m$ space group (space group no. 221). The 'A' cation takes the (0, 0, 0) positions at the 1(a) Wyckoff site, 'B' cation takes the (1/2, 1/2, 1/2) positions at the 1(b) Wyckoff site, while the 'O' anion takes the (1/2, 1/2, 0) positions at the 3(c) Wyckoff site defined in the $Pm\bar{3}m$ space group. The two sketches of the cubic perovskite structures are shown in Fig. 1.1(a) and 1.1(b). However, the real crystal structure of the perovskites depends on the ionic radii of the cations and anions. The measure of the degree of the distortion of a perovskite structure from the ideal cubic structure is defined in terms of the tolerance factor 't', which is given by

$$t = \frac{R_A + R_O}{\sqrt{2}(R_B + R_O)} \qquad (1.1)$$

where R_A, R_B and R_O are ionic radii of A, B and O ions respectively. For t = 1, the structure is expected to adopt the ideal cubic symmetry. For t > 1, the B atom is too small for oxygen octahedron so that the structure will develop a small polar distortion as in $BaTiO_3$. If t is slightly less than one, rotations and tilting of the oxygen octahedral will be favoured as in $SrTiO_3$ and $CaTiO_3$.

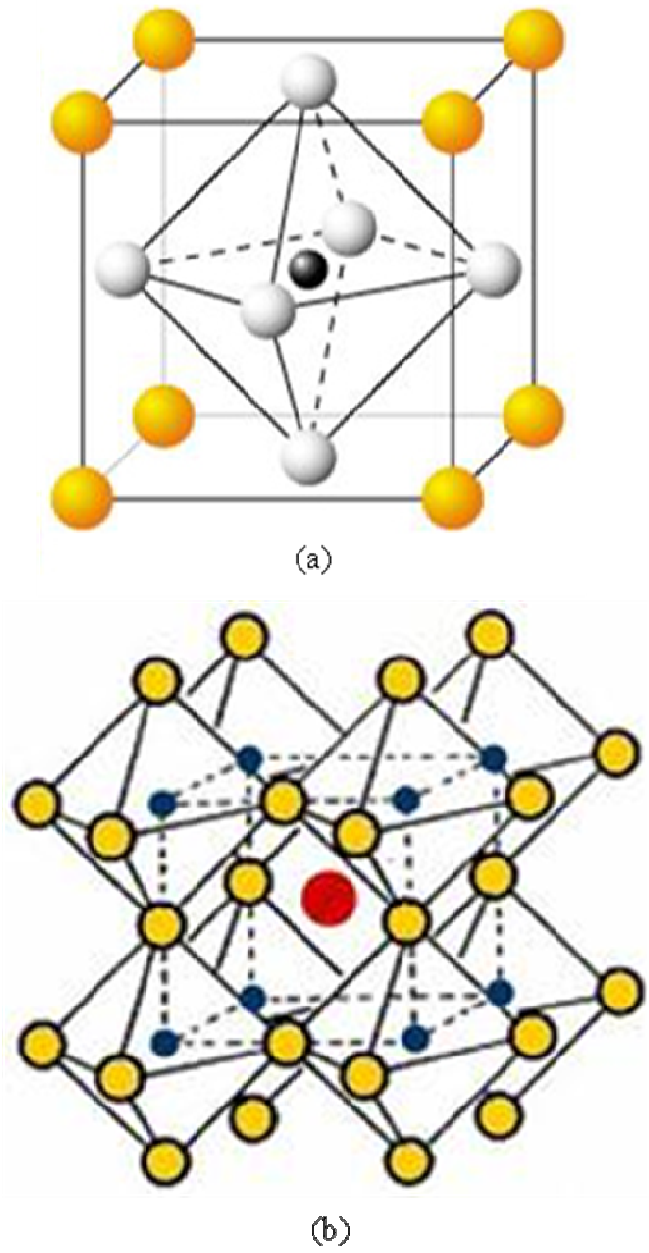

Fig. 1.1 Two typical view of the cubic perovskite structure (a) A cation sits on the cubic corner position (0, 0, 0) (shown by big yellow sphere), B cation sits on the (1/2, 1/2, 1/2) position (shown by small dark sphere) and O anion sits on the face diagonal (1/2, 1/2, 0) positions (shown by medium size white sphere) (b) perovskite structure in the form of BO_6 octahedra, A cation is shown by the big red sphere, B cation is shown by the small dark sphere while the O anion is shown by the yellow circle.

However, for much smaller value of t, the compound will favour a strongly distorted structure with only 6 neighbours for the A atom as in $LiNbO_3$. The perovskite type structures will be unfavourable if the value of the t is very different from unity. For a stable perovskite, the value of t lies in the range $0.80 < t < 1.05$.

1.3 Ferromagnetic and antiferromagnetic materials

Ferromagnetism is defined as the presence of spontaneous magnetization in the absence of an external magnetic field whose orientation can be changed by the applied magnetic field. The origin of the spontaneous magnetization is due to an internal molecular field which tends to align the magnetic moments parallel to each other. The origin of the molecular field has been found to be quantum mechanical exchange energy, which causes electrons with parallel spins (and therefore parallel magnetic moments) to have a lower energy than electrons with antiparallel spins in the ferromagnetic materials. As ferromagnetic materials are heated, the degree of alignment of the atomic magnetic moments decreases i.e. it becomes disordered and the ferromagnetic materials transform to paramagnetic at higher temperatures. The temperature at which this transition takes place is known as the Curie temperature (T_C). Above T_C the susceptibility varies according to the Curie-Weiss law given as

$$\chi = \frac{C}{(T - T_C)} \qquad (1.2)$$

As-prepared samples of ferromagnetic materials often lack a macroscopic magnetization due to the presence of domains of magnetization oriented in different directions. The subsequent alignment and reorientation of the domains,

upon the application of the magnetic field (H), results in a hysteresis in the magnetization (M) and applied magnetic field H as shown in Fig. 1.2.

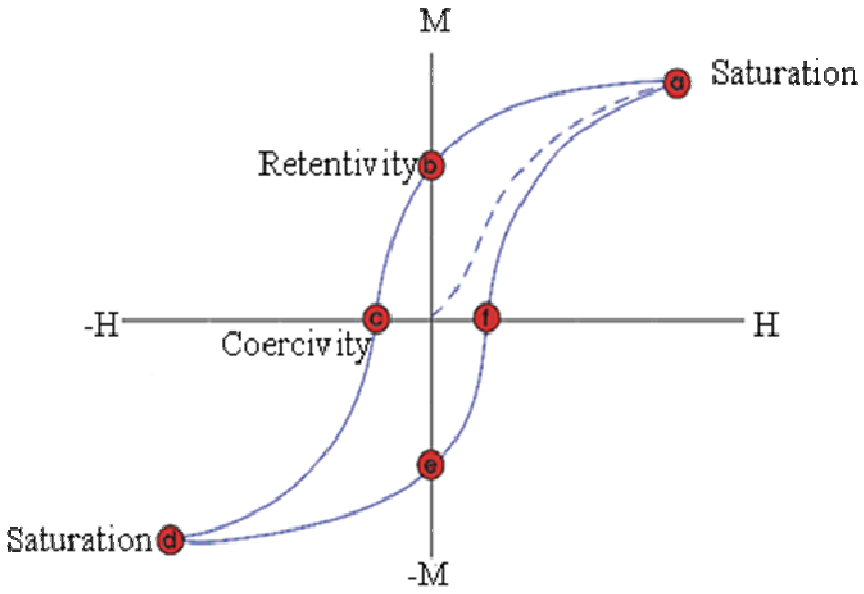

Fig. 1.2 M-H hysteresis loop for the ferromagnetic materials [from http://www.ndt-ed.org/education/resources/communitycollege/mag particle/physics/hysteresis loop.htm].

When the alignment of the spin moments of neighbouring atoms is antiparallel to each other, it is termed as antiferromagnetism**.** No net magnetic moment is associated in this case, since there is a total cancellation of both spin and orbital moments. There are several ways of arranging an equal number of up and down spins depending on the kind of crystal lattice on which the spins are to be arranged. These types of arrangements result in different types of

antiferromagnetic ordering (A-, C-, G-, or E-type) [Wollan et al. (1955)]. Antiferromagnetic order vanishes above a critical temperature known as the Néel temperature. Above the Néel temperature (T_N), the material behaves like a typical paramagnet. Below T_N, due to lower thermal energy as compared to the gain due to antiparallel ordering of neighbouring spins, the antiferromagnetic state is formed. A plot of inverse of susceptibility (χ^{-1}) versus temperature (T) is a straight line in antiferromagnets also, just like ferromagnets, above T_N but this line extrapolates to negative Curie temperature ($-T_C$) at $1/\chi=0$. Above T_N, it obeys the Curie-Weiss law. Although, one does not expect net magnetization in the antiferromagnetic materials, it may exhibit net magnetization due to spin canting, lattice defects, and, frustrated surface spins in the absence of magnetic field. At sufficiently high magnetic fields, the spin direction of one of the magnetic sublattices may rotate and eventually lead to the 'spin flop' where all the spins would be aligned in a parallel fashion. Because of this rotation and spin flop, magnetization can be induced by an external magnetic field. The temperature dependence of the magnetization (M) and χ^{-1} for different types of magnetic materials (ferromagnetic and antiferromagnetic) are shown in Fig. 1.3 (a) and (b).

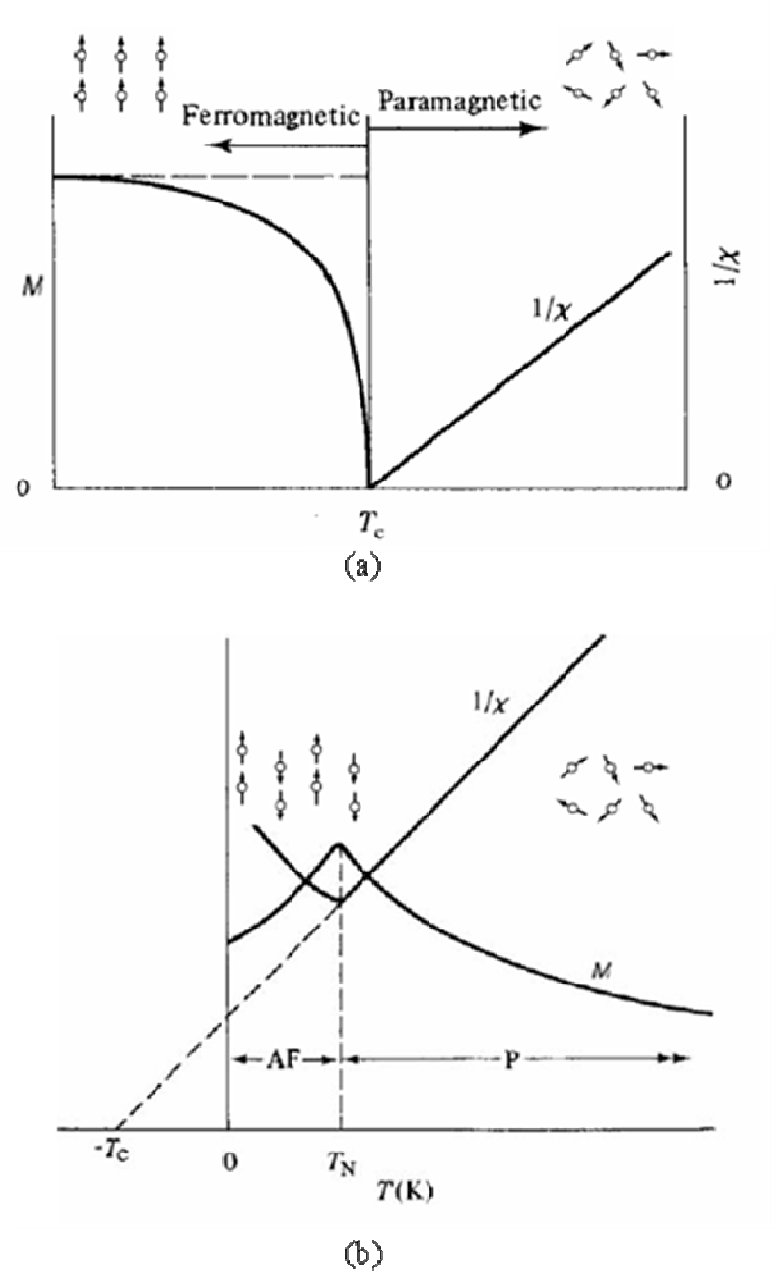

Fig. 1.3 Temperature dependence of the magnetization (M) and inverse of the magnetic susceptibility (χ^{-1}) for (a) ferromagnetic and (b) antiferromagnetic material. AF = Antiferromagnetic and P = Paramagnetic [after Cullity (1972)].

1.4 Magnetic exchange interactions

The nature of the magnetic exchange interactions among the magnetic moments decides whether the material is ferromagnetic or antiferromagnetic. The magnetic interactions between the magnetic moments, which is quantum mechanical in nature, is known as the exchange interaction and is rooted in the overlap of electrons in conjunction with Pauli's exclusion principle. The different types of the magnetic exchange phenomenon which lead to the long range magnetic order state are discussed pointwise as follows.

1.4.1 Direct exchange interaction

The interaction taking place between the neighbouring magnetic ions is known as direct exchange interaction. If the two atoms i and j have spin angular momentum S_i h/2π and S_j h/2π respectively, then the exchange energy between them is given by

$$E_{ex} = -2J_{ex} S_i . S_j = -2 J_{ex} S_i S_j \cos \varphi \qquad (1.3)$$

Where J_{ex} is called the exchange integral, which occurs in the calculation of the exchange effect, and φ is the angle between the spins. If J_{ex} is positive then E_{ex} is minimum when the spins are parallel (cos φ = 1) and a maximum when they are anti-parallel (cos φ = -1). If J_{ex} is negative, the lowest energy state results from antiparallel spins. A positive value of the exchange integral is therefore a necessary condition for ferromagnetism to occur. The nature of the direct exchange interaction can be determined using the Bethe-Slater curve shown in Fig.

1.4 which represents the magnitude and sign of exchange integral (J_{ex}) as a function of inter-atomic distance.

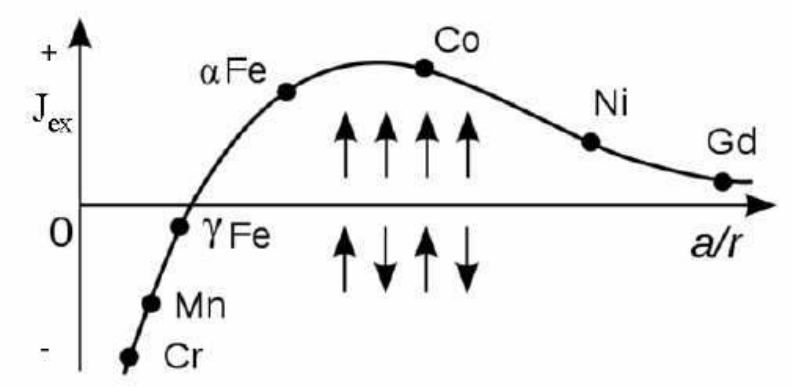

Fig. 1.4 Bethe-Slater curve (schematic). 'a' is the radius of an atom and 'r' the radius of its 3d shell of electrons [after Cullity (1972)].

1.4.2 Indirect exchange interaction

The exchange interaction occurring between the magnetic ions via a non-magnetic anion is known as magnetic indirect exchange interaction. The super exchange and double exchange are two main examples of the indirect exchange interactions. Both the interactions are strongly dependent on the magnetic moment of the magnetic ions, the overlap integral between orbital's of magnetic ions and anions, and the bond angle between the two magnetic ions.

1.4.3 Super exchange interaction

The exchange interaction in antiferromagnetic solids takes place by the mechanism of indirect exchange also called as superexchange interaction. In these structures, the positive metals ion, which carry the magnetic moment, are too far

apart for direct exchange forces to be of much consequences. Instead, they act indirectly through the neighbouring anions. For example, MnO and MnF_2 are both antiferromagnets, though there is no direct overlap between the electrons on Mn^{2+} ions in each system. The exchange interaction in such cases is taking place between non-neighbouring magnetic ions mediated by a non-magnetic ion placed in between the magnetic ions. The strength of the antiparallel coupling between the metal ions M depends on the bond angle ∠M-O-M and is generally greatest when this angle is 180˚ (M-O-M collinear).

1.4.4 Double exchange interaction

In some oxides, it is possible to have a ferromagnetic exchange interaction due to the occurrence of magnetic ions showing mixed valency i.e., it can exist in more than one oxidation state. For example, Mn ion which can exist in oxidation state 3 or 4, i.e. as Mn^{3+} or Mn^{4+}, in the mixed manganite system $La_{1-x}Sr_xMnO_3$. The ferromagnetic alignment in such systems is due to the double exchange mechanism given by Zener (1951). Zener (1951) considered that the intra-atomic Hund rule exchange is stronger and that the carriers do not change their spin orientation when hopping from one ion to the next, so that they can only hop if the spins of the two ions are parallel. For example, consider the 180˚ interaction of Mn-O-Mn in which the Mn "e_g" orbitals are directly interacting with the O "2p" orbitals and one of the Mn ions has more electron than other. In the ground state electron on each Mn ion are aligned according to the Hunds rule. If O gives up its spin-up electron to Mn^{+4}, its vacant orbital can then be filled by an electron from Mn^{+3}. At the end of the process, an electron has moved between the neighboring

metal ions, retaining its spin. The double-exchange predicts that this electron movement from one species to another will be facilitated more easily if the electrons do not have to change spin direction in order to conform to Hunds rules when on the accepting species. The ability to hop, reduces the kinetic energy. Hence the overall energy saving can lead to ferromagnetic alignment of neighboring ions. This model is superficially similar to superexchange. However, in superexchange, a ferromagnetic or antiferromagnetic alignment occurs between two atoms with the same valence (number of electrons); while in double-exchange, the interaction occurs only when one atom has an extra electron compared to the other. Double exchange mechanism schematically shown in Fig. 1.5.

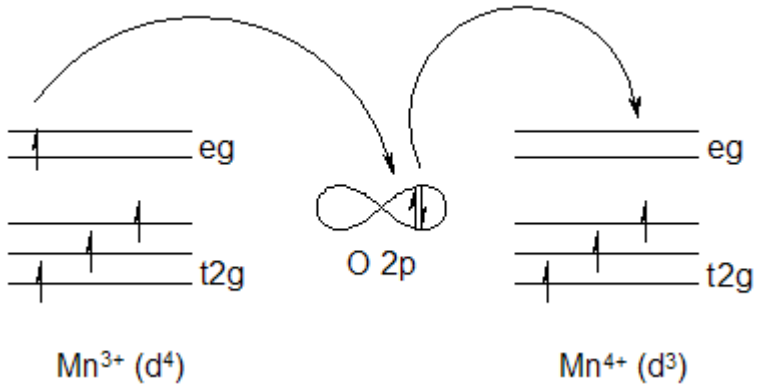

Fig. 1.5 Double exchange mechanism gives ferromagnetic coupling between Mn^{3+} and Mn^{4+} ions participating in electron transfer [http://en.wikipedia.org/wiki/double-exchange_mechanism].

1.4.5 Anisotropic super-exchange interaction

A theory of anisotropic superexchange interaction is developed by extending the Anderson theory of superexchange to include the spin orbit coupling. The weak ferromagnetic moments in antiferromagnet arises when

magnetic moments are canted with respect to each other. It involves the Dzyaloshinskii-Moriya (DM) interaction $D_{1,2}.S_1 \times S_2$, where $D_{1,2}$ is the Dzyaloshinskii vector. The Dzyaloshinskii vector $D_{1,2}$ is proportional to $\lambda x \times r_{1,2}$, where $r_{1,2}$ is a unit vector along the line connecting the magnetic ions 1 and 2, x is shift of the oxygen ion from the line and λ is the spin orbit coupling constant. DM interaction is a relativistic correction to the usual superexchange and its strength is proportional to the spin-orbit coupling constant (λ). The DM interaction favours non-collinear spin ordering. For example, it gives rise to the weak ferromagnetism in antiferromagnetic layers of La_2CuO_4. The spin arrangements in La_2CuO_4 due to DM interaction are shown in Fig. 1.6.

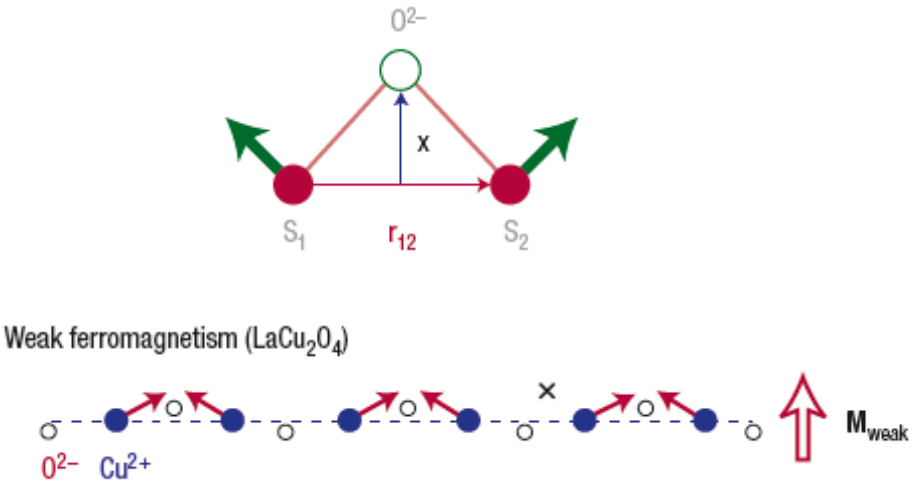

Fig.1.6 Effects of Dzyaloshinskii-Moriya (DM) interaction. Weak ferromagnetism in antiferromagnet La_2CuO_4 layers results from the alternating Dzyaloshinskii vector [After Cheong et al. (2007)].

1.5 Ferroelectricity and Antiferroelectricity

Ferroelectricity is defined as the phenomenon of the presence of spontaneous polarization (P_S) whose direction can be reversed on application of an external electric field. The phenomenon of ferroelectricity is usually observed in polar class of non-centrosymmetric crystal [Jaffe et al. (1971)]. The ferroelectric materials are characterized by their two inherent properties (i) All ferroelectric materials show hysteresis loop between electric polarization and the applied electric field similar to that shown in Fig. 1.7. The hysteresis loop disappears above a certain temperature known as Curie point (T_0). (ii) The temperature dependence of the dielectric constant (ε_r) above the Curie temperature i.e. in paraelectric region is governed by the Curie-Weiss law,

$$\varepsilon_r = \frac{C}{(T - T_C)} \qquad (1.4)$$

where ε_r is the real part of the dielectric constant of the material. T_C (Curie temperature) is obtained by extrapolation of $1/\varepsilon_r$ vs. temperature plot. For second order ferroelectric phase transitions the Curie point and Curie temperature are identical i.e. $T_C = T_0$. In the case of a first order ferroelectric phase transition, the Curie temperature and Curie point are not identical but Curie temperature (T_C) is lower than Curie point (T_0) [Lines and Glass (1977)].

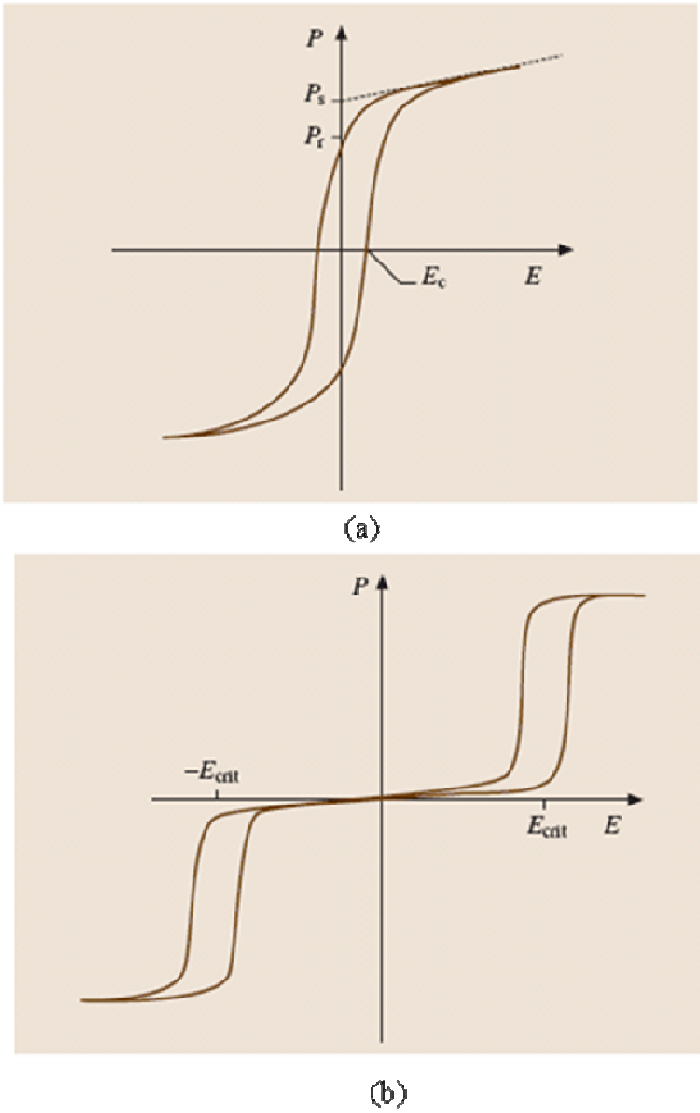

Fig. 1.7 Hysteresis loop for (a) ferroelectric and (b) antiferroelectric materials (after Martienssen and Warlimont 2005).

Antiferroelectric (AFE) materials do not show spontaneous macroscopic polarization but do have sublattice polarization. On the application of a sufficiently high electric field a macroscopic polarization can be made to develop in the antiferroelectric material. Unlike FE materials, one observes “twin” P-E

hysteresis loops in AFE materials as shown in Fig. 1.7 The example of the antiferroelectric materials are $PbZrO_3$ and $NaNbO_3$. The polar arrangement in antiferroelectrics can be visualized as two sub-cells polarized in opposite directions giving rise to a center of symmetry and a net zero polarization. The transition temperature is commonly known as Néel temperature for these materials in analogy with the Néel temperature of antiferromagnetic materials.

1.6 Magnetoelectric coupling in multiferroics

The magnetoelectric effect, describes the coupling between electric and magnetic fields in matter i.e. induction of magnetization (M) by an electric field (E) and polarization (P) by a magnetic field (H). Thermodynamically, the magnetoelectric effect can be understood within the Landau theory frame work, approached by the expansion of the free energy for the magnetoelectric system [Fiebig (2005); Wang et al. (2009)] i.e.

$$F(E,H) = F_0 - P_i^s E_i - M_i^s H_i - \tfrac{1}{2}\varepsilon_0 \varepsilon_{ij} E_i E_j - \tfrac{1}{2}\mu_0 \mu_{ij} H_i H_j$$

$$- \alpha_{ij} E_i H_j - \tfrac{1}{2}\beta_{ijk} E_i H_j H_k - \tfrac{1}{2}\gamma_{ijk} H_i E_j E_k \quad -..... \quad (1.5)$$

where F_0 is the ground state free energy, subscripts (i,j,k) refer to the three components of a variable in spatial coordinates, E_i and H_i the components of the electric field E and magnetic field H respectively, P_i^s and M_i^s are the components of the spontaneous polarization (P^s) and the spontaneous magnetization (M^s), μ_0 and ε_0 are the magnetic and dielectric susceptibilities of vacuum, μ_{ij} and ε_{ij} are the second order tensors of magnetic and dielectric susceptibilities, β_{ijk} and γ_{ijk} are the

third order tensor coefficients and α_{ij} is the components of tensor α which is designated as the linear magnetoelectric effect and corresponds to the induction of the polarization by a magnetic field or magnetization by an electric field. The rest of the terms in the preceding equations correspond to the higher order magnetoelectric effects parameterized by tensors β and γ. The magnetoelectric effects can then easily be established in the form $P_i(H_j)$ or $M_i(E_j)$. Both are obtained by differentiating equation (1) w. r. t. E_i or H_i and then setting E_i or $H_i = 0$ we get

$$P_i = \alpha_{ij} H_j + \frac{\beta_{ijk}}{2} H_j H_k + \ldots\ldots\ldots \qquad (1.6)$$

$$\mu_0 M_i = \alpha_{ji} E_j + \frac{\gamma_{ijk}}{2} E_j E_k + \ldots\ldots\ldots \qquad (1.7)$$

1.7 Incompatibility between ferroelectricity and magnetism

In the light of the symmetry consideration, ferroelectricity needs the broken spatial inversion (x,y,z→-x,-y,-z) symmetry while the time reversal symmetry can be invariant. A spontaneous polarization would not appear unless a structure distortion of high symmetry paraelectric phase breaks the inversion symmetry. The conventional ferroelectric oxides contain transition metal (TM) ions with a formal configuration d^0, such as Ti^{4+}, Nb^{5+}, Ta^{5+} and W^{6+} at the B-sites (i.e. transition metals ions with an empty d-shell). The empty d-shell seems to be a prerequisite for ferroelectricity generation, although this does not mean that all perovskite oxide with d^0 TM ions must exhibit ferroelectricity. Magnetism, in contrast, requires TM ions at the B-site with partially filled (d^n) shells such as

Cr^{3+}, Mn^{3+} and Fe^{3+}, because the spins of electrons occupying the filled d-shell completely add to zero magnetic moment and do not participate in the magnetic ordering. The difference in filling TM ions d-shell at the B-site, which is required for ferroelectricity and magnetism, makes these two ordered states mutually exclusive [Hill et al. (1999), Hill (2000), Wang et al. (2009)].

1.8 Approaches to the co-existence of the ferroelectricity and magnetism

Ferroelectric perovskite oxides need B-site TM ions with empty d^0-shell to form ligand hybridization with the surrounding anions. This type of electronic structure excludes magnetism. While this argument suggests that ferroelectricity and magnetism are incompatible, new mechanisms of ferroelectricity, different from the conventional one have been identified in recent years which make mutually exclusive phenomena occur in the same material.

1.8.1 Mixing of the magnetic TM ions (d^n) with ferroelectrically active TM (d^0) ions

The first route towards perovskite multiferroics was taken by Russian researchers. They proposed to mix both magnetic TM ions with d^n electrons and ferroelectrically active TM ions with d^0 configuration at the B-site. It was expected that the magnetic ions and d^0-shell TM ions favour separately a magnetic order and a ferroelectric order. This idea has worked and multiferrocity has been reported in compound $Pb(Fe_{0.5}Nb_{0.5})O_3$ (PFN) in which Nb^{5+} ions are ferroelectrically active and Fe^{3+} ions are magnetically active, respectively [Fiebig

(2005), Wang et al. (2009), Singh et al.(2010)]. Theoretical predictions along with experimental results have confirmed the ferroelectric Curie temperature of ~ 385 K [Plantov et al. (1970)] and magnetic Néel temperature of ~ 143 K [Bokov et al. (1962), Bhatt et al. (2004)].

1.8.2 Ferroelectricity induced by lone-pair electrons

The Bi^{3+} and Pb^{2+} ions have two valence electrons in their s-orbit which belong to the lone pairs. The lone pair state is unstable and will invoke a mixing between the ns^2 ground state and a low –lying $(ns)^1(np)^1$ excited state, which eventually leads these ions to break the inversion symmetry. This stereochemical activity of the lone pair helps to stabilize the off-center distortions and in turn ferroelectricity. The ions with lone pair electrons such as Bi^{3+} and Pb^{2+} always locate at A-site in an ABO_3 perovskite structure. This allows the magnetic TM ions at the B-sites so that incompability for TM ions to induce both magnetism and ferroelectricity is partially avoided. The typical examples are $BiFeO_3$ and $BiMnO_3$, where the B-site ions contribute to the magnetism and A-site ions via the lone pair mechanism lead to the ferroelectricity. In both $BiFeO_3$ and $BiMnO_3$, Bi^{3+} ions with two electrons in a 6s orbit (lone pair) shift away from the centrosymmetric positions with respect to the surrounding oxygen ions, favouring the ferroelectricity. Magnetism is due to the Fe^{3+} and Mn^{3+} ions.

1.9 Multiferroic materials with improper ferroelectricity

In the preceding section, it has been discussed that main driving force for the ferroelectric transition comes from the structural instability toward the polar

state associated with the electronic pairing. These ferroelectrics are termed as 'proper' ferroelectrics. There are some other types of the ferroelectrics in which polarization induced by product of the complex lattice distortions. This class of materials, together with all other ferroelectrics with their polarization originating from by-product of other order configurations was termed as 'improper' ferroelectrics. Some example of the proper and improper ferroelectricity is given in the Table 1.1 [After Cheong and Mostovoy (2007)].

1.9.1 Geometric ferroelectricity in Hexagonal manganites

In rare-earth hexagonal manganites $RMnO_3$ (R, rare-earth element like Ho, Lu or Y) ferroelectricity arises as a result of by-product of a complex lattice distortion. In this category of manganites, $YMnO_3$ is most studied one. The Mn^{3+} ions in $YMnO_3$ is coordinated by a five-fold symmetry (i.e. in the centre of O_5 trigonal bipyramid) in contrast to conventional perovskites, in which B-site cation lies inside the O_6 octahedra.

Table 1.1 Classification of ferroelectrics [after Cheong et al. (2007)].

	Mechanism of inversion symmetry breaking	Materials
Proper	Covalent bonding between $3d^0$ transition metal (Ti) and oxygen	$BaTiO_3$
	Polarization of $6s^2$ lone pair of Bi or Pb	$BiMnO_3$, $BiFeO_3$, $Pb(Fe_{2/3}W_{1/3})O_3$
Improper	Structural transition 'Geometric ferroelectrics'	K_2SeO_4, Cs_2CdI_4 hexagonal $RMnO_3$
	Charge ordering 'Electronic ferroelectrics'	$LuFe_2O_4$
	Magnetic ordering 'Magnetic ferroelectrics'	Orthorhombic $RMnO_3$, RMn_2O_5, $CoCr_2O_4$

The ferroelectric phase of $YMnO_3$ has $P6_3cm$ space group symmetry and magnetic moment of Mn^{3+} forms an A-type antiferromagnetic (non-collinear order) [Bertaut et al. (1963)]. The structural phase transition from the paraelectric (centrosymmetric) $P6_3/mmc$ to the ferroelectric $P6_3cm$ is obtained by two types of atomic displacements. First one is the MnO_5 bipyramids buckleing that results in a shorter c-axis and the O_T^{2-} (in plane) ions are shifted towards two longer Y^{3+}-O_P^{2-} (perpendicular to bipyramids plane) bonds. Second ion is the vertical shift of the Y^{3+} ions away from the high temperature mirror plane perpendicular to the hexagonal c-axis, keeping the constant to O_T^{2-} ions. The main difference between the PE $P6_3/mmc$ structure and ferroelectric $P6_3cm$ structure is that, in the PE phase all ions are restricted within the planes parallel to the ab plane, whereas in the ferroelectric $P6_3cm$ phase, the mirror planes are lost. Consequently, one of the two equal Y-O_P bonds (~ 2.8Å) is reduced down to ~ 2.3Å and other is elongated to 3.4Å, leading to a net electric polarization [Aken et al. (2004)]. The polarization – dependent X-ray absorption spectroscopy (XAS) at 0 K and Mn L2,3 edges of $YMnO_3$ demonstrated that the Y 4d states are indeed strongly hybridized with the O 2p states and this results in large anomalies in the Born effective charges on the off-centered Y and O ions [Cho et al. (2007)]. Thus the main dipole moments are contributed by the Y-O pairs instead of the Mn-O pairs. Interestingly, the huge Y-O_P off-centre displacements are quite distinct from the small displacements induced by chemical activity available for conventional ferroelectric perovskite oxides, but the induced electric polarization remains much smaller [Kang et al. (2005), Fennie et al. (2005)].

Coupling between the ferroelectric and antiferromagnetic orders in $YMnO_3$ had been investigated by different workers [Huang et al. (1997), Lee et al. (2005)]. In a recent report, Lee et al. (2008) have shown that the hexagonal manganites including $YMnO_3$ undergo an isostructural transition at T_N, simultaneously producing giant atomic displacements for every atom in the unit cell. Lee et al. have predicted that the extremely large magneto-elastic coupling, is the primary origin of multiferroic phenomenon in hexagonal manganites.

1.9.2 Ferroelectricity in charge order system

Ferroelectricity in charge ordered system originates from the electronic correlation rather than the covalency. In many narrowband metal oxides, like in $LuFe_2O_4$, charge carriers become localized at low temperature and form a periodic non-symmetric charge order structure (i.e. CO state) [Portengen et al. (1996), Ikeda et al. (2005), Xiang et al. (2007), Zhang et al. (2007), Christianson et al. (2008a and b), Nagano et al. (2007), Subramanian et al. (2006)]. At room temperature, $LuFe_2O_4$ has a hexagonal layered structure with an alternative stacking of triangular lattices of rare-earth elements irons and oxygens. Each Fe_2O_4 layer is made up of two triangular sheets of corner-sharing FeO_5 trigonal bipyramids and equal number of Fe^{2+} and Fe^{3+} ions co-exists on the same site of the triangular lattice. With respect to the average $Fe^{2.5+}$ valence, Fe^{2+} and Fe^{3+} ions are considered to be an excess and a deficient half electron state respectively. Due to the Coulomb force, oppositely signed charges Fe^{2+} and Fe^{3+} pair up and then the charge-ordered state gets stabilized. The charge order pattern of alternating Fe^{2+}: Fe^{3+} layers with ratios of 2:1 and 1:2 appears at around 370 K. This CO structure

allows the presence of a local electric polarization. Experimentally electric polarization of ~ 26μC/cm^2 was measured using the pyroelectric current method [Portengen et al. (1996), Ikeda et al. (2005)].

1.9.3 Spiral spin order induced ferroelectricity

The microscopic mechanism inducing ferroelectric polarization in magnetic spirals involves the antisymmetric Dzyaloshinskii-Moriya (DM) interaction $D_{n,n+1}.S_n \times S_{n+1}$, where $D_{n,n+1}$ is the Dzyaloshinskii vector [Moriya (1960), Dzyaloshinskii (1964)]. This interaction is a relativistic correction of a usual super-exchange interaction and its strength of coupling is proportional to the spin orbit coupling constant. The Dzyaloshinskii vector $D_{n,n+1}$ is proportional to x $\times$ $r_{n,n+1}$, where $r_{n,n+1}$ is a unit vector along the line connecting the magnetic ions n and n+1, and x is the shift of the oxygen ion from this line (see Fig. 1.8). Thus, the energy of the DM interaction increases with x, and describing the degree of inversion symmetry breaking at the oxygen site. Because in the spiral state the vector product $S_n \times S_{n+1}$ has the same sign for all pairs of neighbouring spins, the DM interaction pushes negative oxygen ions in one direction perpendicular to the spin chain formed by positive magnetic ions, thus inducing electric polarization perpendicular to the chain [Sergienko I. A. & Dagotto E. (2006)].

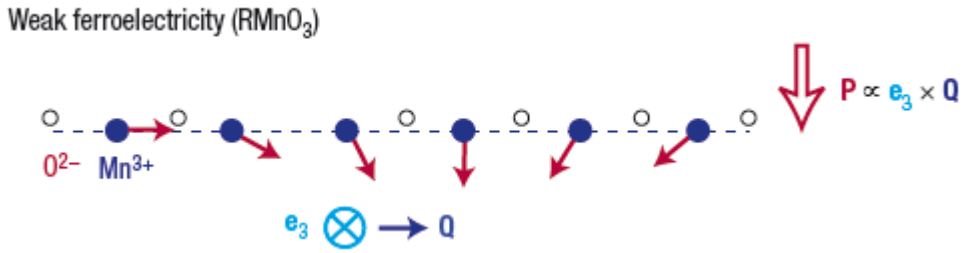

Fig.1.8 Weak ferroelectricity can be induced by the exchange-striction effect in the magnetic spiral state, which pushes the oxygen ion in one direction transverse to the spin chain formed by the magnetic ions.

1.10 Structure and multiferroic properties of $BiFeO_3$

The crystal structure of $BiFeO_3$ at ambient temperature is rhombohedrally distorted perovskite structure with the R3c space group [Jacobson et al. (1975); Fischer et al. (1980); Kubel (1990); Sosnowska et al. (2002)]. The hexagonal lattice parameter are $a_{hex}=b_{hex}=5.58102(4)$, $c_{hex}=13.8757(4)$, $\alpha=\beta=90^{\circ}$ and $\gamma=120^{\circ}$ [Palewicz et al. (2007)]. The hexagonal unit cell contains six formula units whereas rhombohedral unit cell, shown in Fig. 1.9, contains two formula units arising from counter-rotations of neighboring oxygen octahedra about the trigonal $[111]_{pc}$ axis. The *R*3*c* symmetry permits the development of a spontaneous polarization along $[111]_{pc}$, and Bi, Fe, and O are displaced relative to one another along this threefold axis [Palewicz et al. (2007)].

From experimental point of view, the characterization of the ferroelectric behaviour of $BiFeO_3$ at room temperature has proven to be a very difficult task, which comes from the high conductivity of $BiFeO_3$. Because of this leakage

problem, despite the large ionic displacements in the ferroelectric phase and high ferroelectric Curie temperature, early measurements on bulk single crystal yielded rather small polarization. Teague el al. (1970) initially reported a spontaneous polarization value of only 6.1 $\mu C/cm^2$ as measured along the $[111]_{pc}$ polar direction on $BiFeO_3$ single crystals at liquid nitrogen temperature. This value is significantly lower than the value expected based on the structural data. Recently, very high value of P_s ~55 $\mu C/cm^2$ (see Fig. 1.10) [Wang et al. (2003)] and 150 $\mu C/cm^2$ [Yun et al. (2004)] have been reported on $BiFeO_3$ thin films. The much higher polarization values measured on thin films over bulk $BiFeO_3$ was initially attributed to the structural change since the symmetry of the $BiFeO_3$ thin films was found to become pseudo-tetragonal (strictly speaking monoclinic) due to the strain introduced by the electrode or the substrate. Initially first-principles calculations have shown that the spontaneous polarization of even the rhombohedral structure of $BiFeO_3$ can reach 90–100 $\mu C/cm^2$ [Neaton et al. (2005); Ravindran et al. (2006)]. More recently, polarization values as high as 100 $\mu C/cm^2$ has been reported [Lebeugle et al. (2007)] along the polar $[111]_{pc}$ direction on $BiFeO_3$ single crystal. The crystals were grown from a Bi_2O_3-Fe_2O_3 flux with a low growth temperature of 1123 K. This work shows that the high polarization is an intrinsic property of $BiFeO_3$, rather than a strain-induced effect, as reported in $BiFeO_3$ thin films.

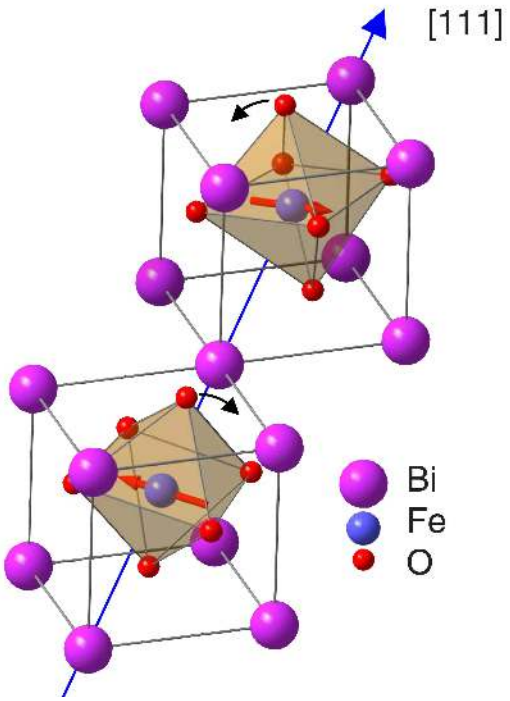

Fig.1.9 Crystal structure of bulk $BiFeO_3$ at room temperature. Two simple perovskite unit cell are shown to illustrate that the successive oxygen octahedra along the polar [111] axis rotate with opposite sense. Arrows on Fe atoms indicate the orientation of the magnetic moments in the (111) plane [after Lubk et al. (2009)].

Apart from ferroelectric behaviour, $BiFeO_3$ is also known to exhibit an antiferromagnetic ordering. Sosnowska et al. (1982) studied the magnetic structure of $BiFeO_3$ and showed that the Fe magnetic moments are coupled ferromagnetically within the pseudocubic $[111]_{pc}$ planes and antiferromagnetically between adjacent planes, as shown in Fig 1.11. This magnetic order corresponds to G-type antiferromagnetic structure with respect to the elementary perovoskite cell. If the magnetic moments are oriented perpendicular to the $[111]_{pc}$ direction (i.e. in the $(111)_{pc}$ plane, the symmetry also permits canting of the magnetic moments due

to Dzyaloshinski-Moriya intraction resulting in macroscopic magnetization, the so-called weak ferromagnetism.

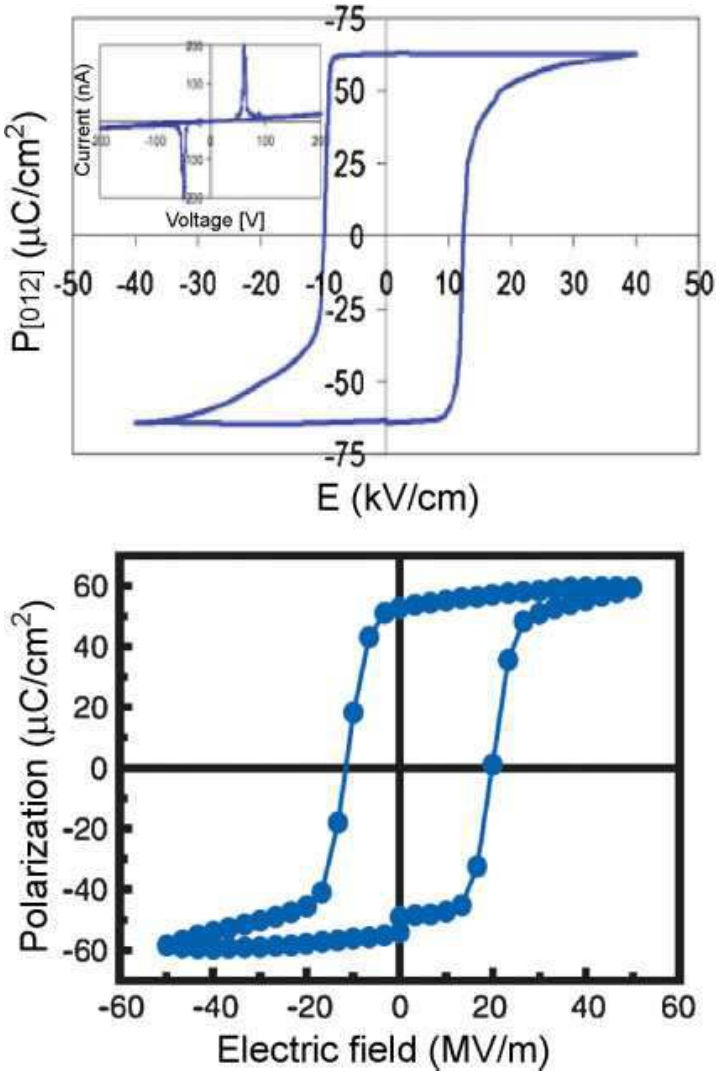

Fig.1.10 Ferroelectric hysteresis loop measured (a) for $BiFeO_3$ single crystal (b) for thin film grown on (100) oriented substrate $SrTiO_3$ at 15 kHz [after Wang et al. (2003)].

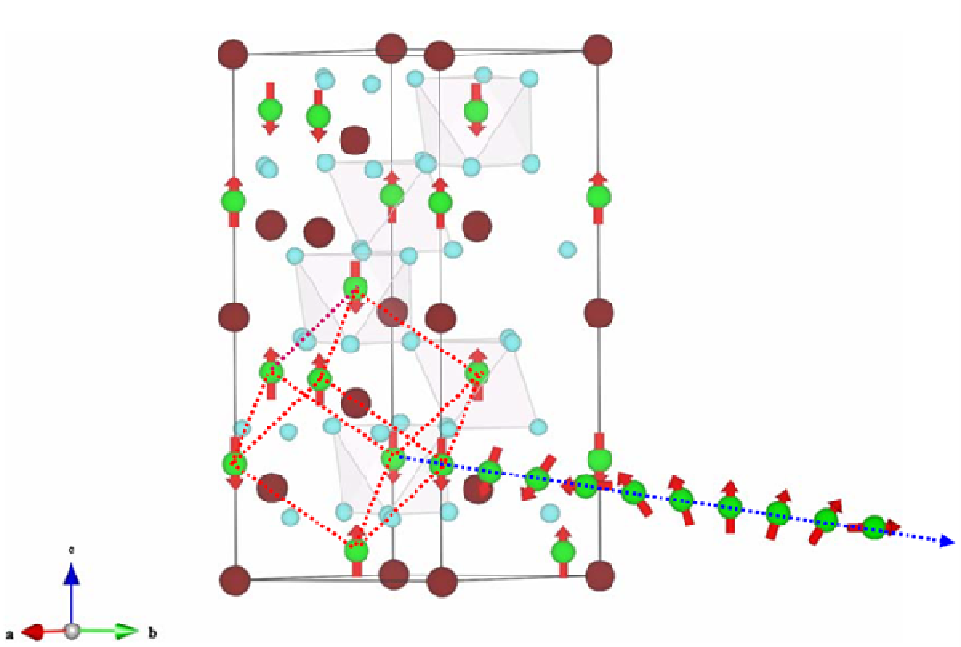

Fig.1.11 $BiFeO_3$ lattice with bismuth (large circles), iron (large circles with arrow) and oxygen ions (small circles) are shown in hexagonal settings [after Park et al. (2011)]. The arrow at the Fe sites indicates the magnetic moments. The magnetic cell (dashed lines) is shown for a G-type antiferromagnetic structure. The propagation wave vector of the incommensurate spiral spin structure k is along the $[110]_h$ direction and lies in the plane of spin rotation $(1\text{-}10)_h$.

However, it was also found that superimposed on the antiferromagnetic ordering, there is a spatially modulated spiral spin structure in which the antiferromagnetic axis rotates through the crystal with an incommensurate long-wavelength period of ~620 Å (see Fig. 1.11) [Sosnowaska et al. (1982)]. The propagation wave vector k is along the $[110]_h$ direction and lies in the plane of spin rotation $(1\text{-}10)_h$ as shown in Fig. 1.11. The existence of the modulated magnetic ordering in $BiFeO_3$ has also

been supported by NMR [Zalessky et al. (2000); Kozheev et al. (2003)] and EPR [Ruette et al. (2004)] studies.

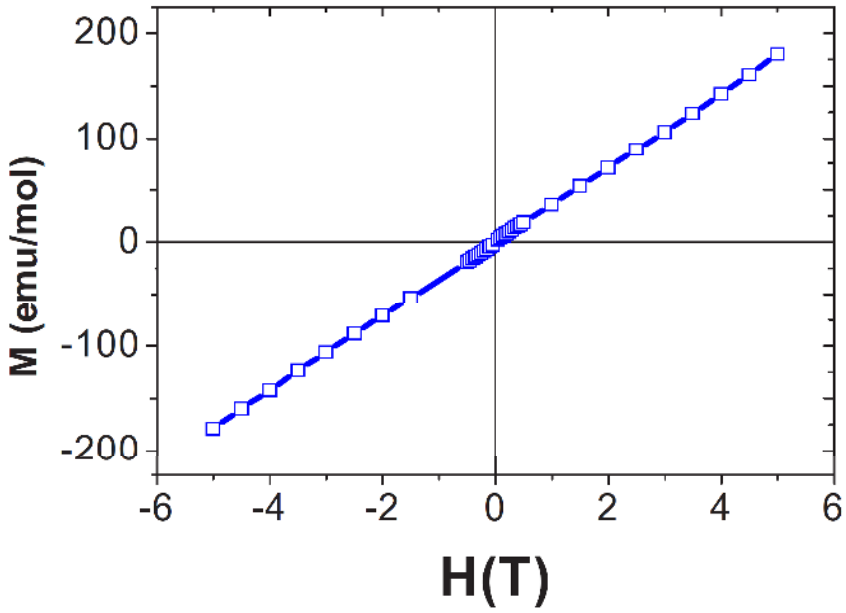

Fig.1.12 Magnetization curve versus applied magnetic field of the powder sample measured at room temperature [after Lebeugle et al. (2007)].

The spiral modulated spin structure leads to cancellation of any macroscopic magnetization due to canting. Owing to the presence of spiral spin structure, the field and temperature dependent magnetization measurements revealed a pure antiferromagnetic response [Lebeugle et al. (2007)] as shown in Fig. 1.12, without any trace of weak ferromagnetism in pure $BiFeO_3$ single crystal. Weak ferromagnetism reported in pure $BiFeO_3$ samples in polycrystalline form [Zhang et al. (2005)] is mostly due to the presence of some magnetic impurity.

1.11 Electric field induced spin-flop in $BiFeO_3$

The scattering studies by Lebeugle et al. (2008) shows the effect of only one propagation vector $k_2 = \delta(1, 0, -1)$ on the intensity distribution from the magnetic reflection. Lebeugle et al. had investigated intensity distribution across $(1/2\text{-}1/21/2)_{pc}$ type antiferromagnetic reflection and shown that the splitting occurs only along $k_2 = \delta(1, 0, -1)$ direction. The reported intensity distribution across $(1/2\text{-}1/21/2)_{pc}$ reflection and the spiral structure is shown in Fig. 1.13.

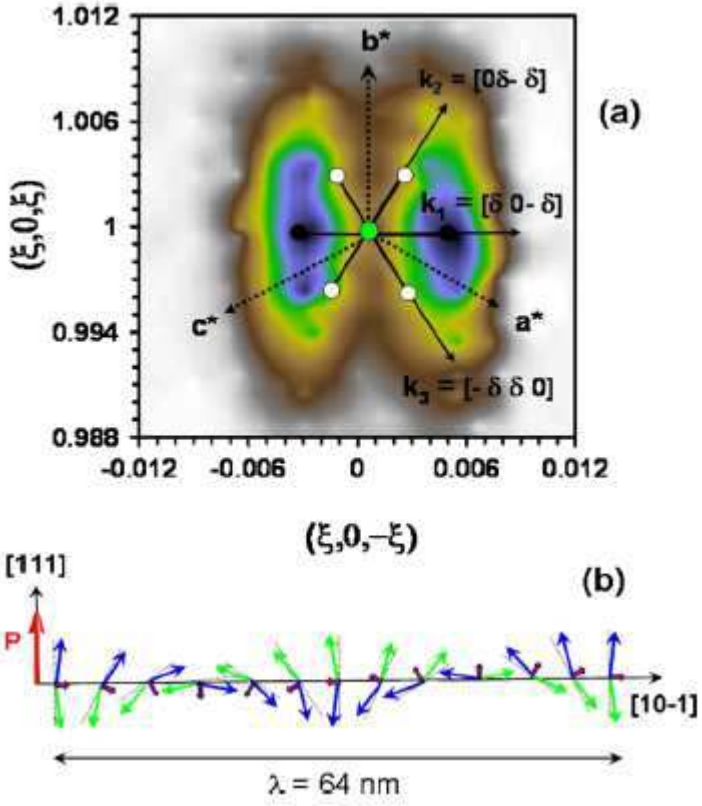

Fig. 1.13 (a) Neutron intensity around the (1/2-1/21/2) Bragg reflection in the virgin, single domain state. Two diffraction satellites indicate that the cycloid is along the [10-1] direction. (b) Schematics of the 640 Å antiferromagnetic circular cycloid [after Lebeugle et al. (2008)].

Lebeugle et al. (2008) have also investigated the effect of poling along $[010]_{pc}$ direction on the neutron scattering intensity distribution.

Mapping of the neutron intensity determined by Lebeugle et al. (2008) from the poled crystal in reciprocal space is shown in Fig. 1.14. In this figure, yellow (or light gray) (111) type reflections are purely nuclear in origin while the red (or gray) (1/21/21/2) are purely magnetic. It is clear that (111) and (1-11) reflections are split along the long diagonals (dashed lines), which according to Lebeugle et al. (2008) indicates the presence of two domains with different interplane distances. These are two rhombohedral twins with polarization axes along [111] and [1-11], 45%-55% in volume [Lebeugle et al. (2008)]. In this context it should be mentioned that, BFO, in rhombohedral phase with R3c space group symmetry, exhibits four structural variants (ferroelastic domain) based on the four different cubic body diagonals and eight possible direction of P (ferroelectric domains). The buckling of the crystal, showing the multidomain state that consists of stripe regions with two different polarization directions schematically shown in Fig. 1.14(a). The strongest $(1/2\text{-}1/21/2)_{pc}$ antiferromagnetic reflection is shown in the zoomed region of Fig.1.14(b) is composed of four spots. According to Lebeugle et al. these result from two simultaneous splits, one due to the ferroelectric distortion (already evidenced in the nuclear peaks) and one of magnetic origin. A projection of the zoomed area is represented in Fig. 1.15 on which green spots indicate the expected reflections from $\sim P_{111}$ (low half of the pattern) and $\sim P_{1\text{–}11}$ (upper half where the polarization rotated by 71º under poling) domains.

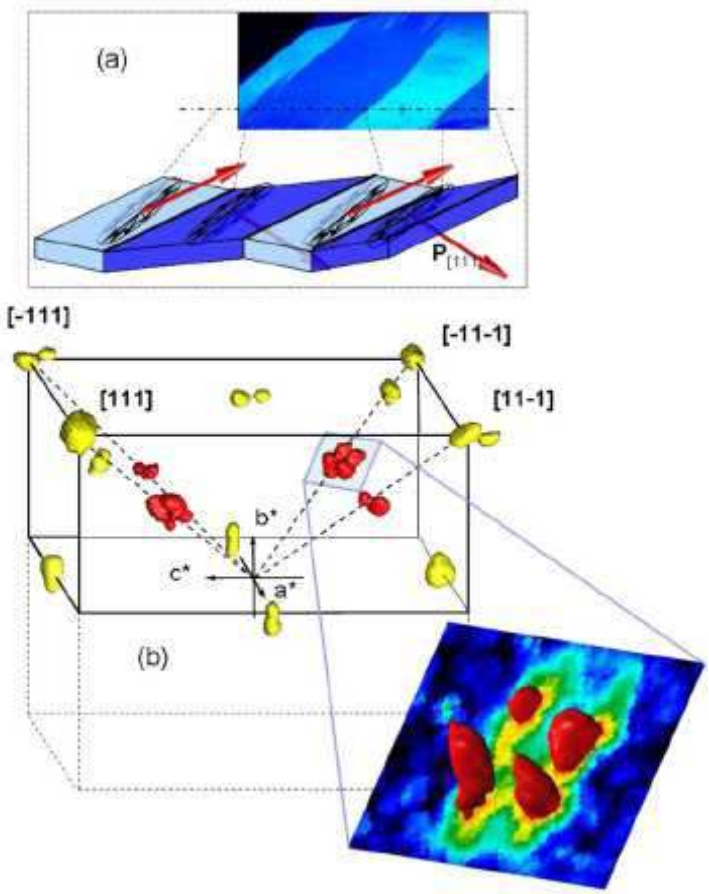

Fig. 1.14 Mapping of the neutron intensity in reciprocal space. Two sets of splitting appear for the nuclear intensity (yellow or light gray spots) due to the presence of two ferroelastic domains [see (a)]: on because of the presence of two rhombohedral distortions along [111] and [1-11], and second because of a physical buckling of the crystal induced by the twinning. Magnetic peaks are further split because of the cycloids [after Lebeugle et al. (2008)].

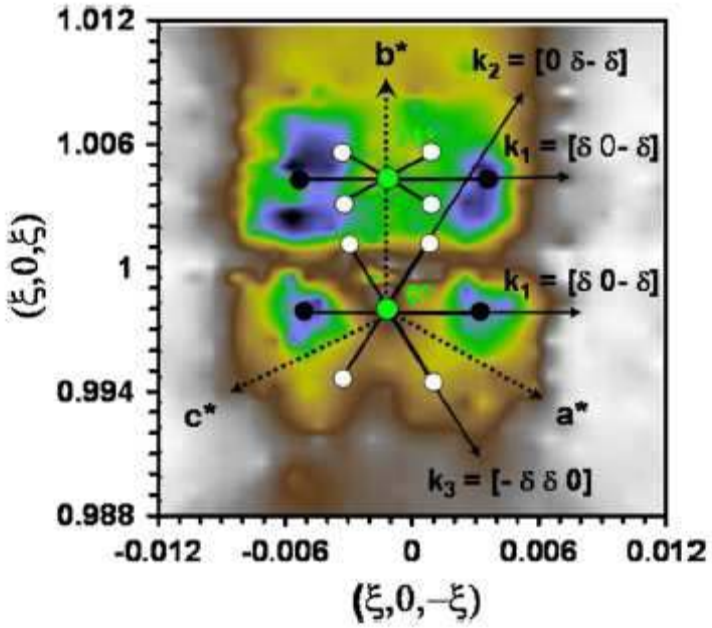

Fig. 1.15 Neutron intensity around the (1/2-1/21/2) Bragg position in the multidomain state. Theoretical positions are indicated by the black and white spots. Diffraction satellites are visible in the 0º (bottom half) and 71º (top half) domains of polarization [after Lebeugle et al. (2008)].

The magnetic satellites in the figure are also indicated as black spots for the cycloid in the original [101] direction and white spots for the other two symmetry allowed ones. The rotation planes of the AF vectors in the two domains was determined by the authors [Lebeugle et al. (2008)] using the integrated intensities of the magnetic reflections and have conclude that 55% of the crystal volume has switched its polarization by 71º, and brought with it the rotation plane of the Fe moments, thus inducing a spin flop of the antiferromagnetic sublattice. In each domain, AF moments make a cycloid by rotating in the plane defined by k_1 and P

and the orientation is represented in Fig. 1.16. According to the Lebeugle et al. this unambiguously demonstrates that the magnetic Fe^{3+} structure is intimately linked to the polarization vector. Although <M> = 0 imposes a zero global linear ME effect, the coupling between M and P at the atomic level still exists [Lebeugle et al. (2008)].

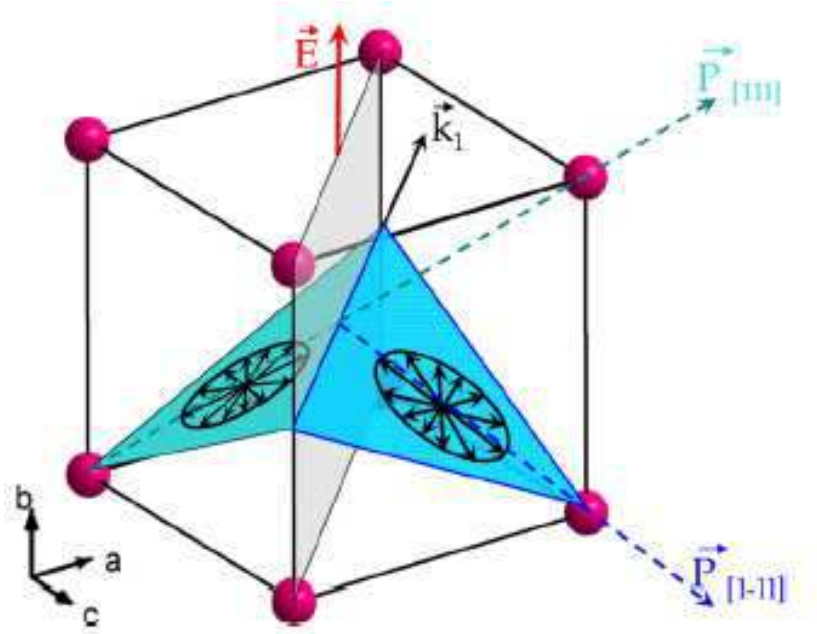

Fig. 1.16 Schematics of the planes of spin rotations and cycloids k~1 vector for the two polarization domains separated by a domain wall (in light gray) [after Lebeugle et al. (2008)].

1.12 High temperature β and γ phases of $BiFeO_3$

Despite extensive studies on bulk $BiFeO_3$, there are still many contradictions about the high-temperature phases. The most complete study of the phase diagram of $BiFeO_3$ has been carried out by Palai et al. (2008) based on

thermal analysis, spectroscopic, diffraction and other methods. They suggest three distinct solid phases above room temperature and below the melting point (1233 K): the rhombohedral α-phase, below T_C, an intermediate β-phase, in the region 1103–1198 K, and a cubic γ-phase in the region 1198–1206 K before decomposition and subsequent melting. Based on both Raman and polarized light measurements they proposed that the symmetries of β and γ phases are orthorhombic and cubic, respectively [Palai et al. (2008)] in disagreement with other recent work suggesting a cubic symmetry for β-phase [Haumont et al (2006)]. First principles calculations predicted that above T_C the structure adopts a tetragonal phase (space group I4/mcm) which is associated with antiferrodistortive motions, before transforming to a cubic phase at approximately 1440 K [Kornev et al.(2007)]. From a high temperature XRD study, these authors have proposed a high temperature monoclinic phase with pseudotetragonal character in the space group C2/m [Haumont et al. (2008)]. A follow-up paper suggested the true space group as $P2_1/m$ [Haumont et al. (2008)]. In another recent high temperature XRD study, Selbach et al. (2008) observed a first order phase change at T_C and proposed that the paraelectric β-phase corresponds to the rhombohedral symmetry with centrosymmetric, space group $R\bar{3}c$. However, more recently, the high temperature neutron diffraction results of Arnold et al. (2009) suggest that the β phase exhibits orthorhombic symmetry in the space group Pbnm. The evolution of the diffraction patterns with temperature as reported by Arnold et al. (2009) are shown in Fig. 1.17. In another high temperature neutron diffraction study, Arnold et al. (2010) proposed Pbnm space group for the γ-phase too. Thus the stability of the

rhombohedral phase of $BiFeO_3$ and its phase transition to the paraelectric state is still controversial.

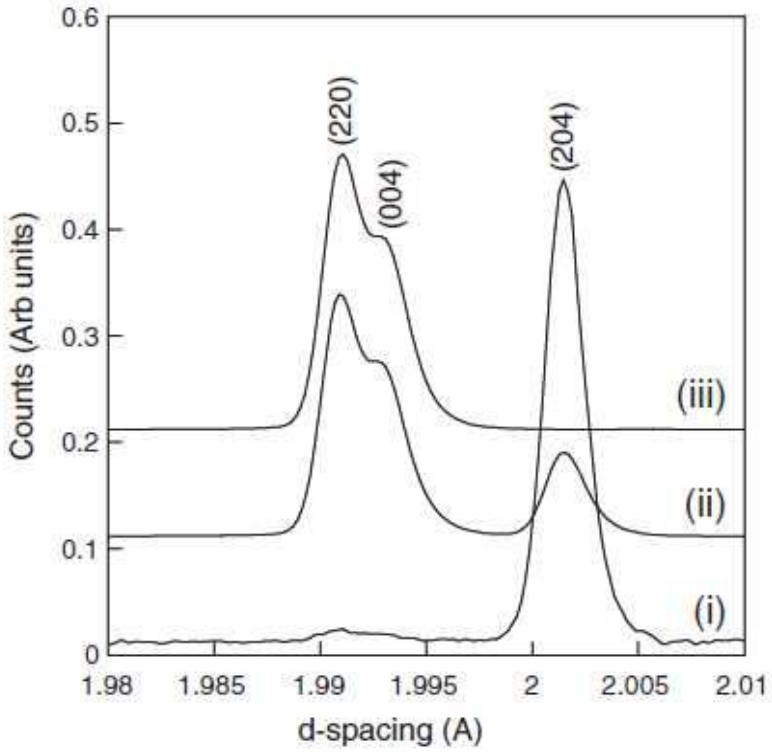

Fig. 1.17 The neutron diffraction profiles of BF at (i) 820º C, (ii) 825º C and (iii) 830º C temperature showing the gradual modification in 200 pseudocubic reflection. The indices are shown in (i) hexagonal and (iii) orthorhombic setting respectively [After Arnold et al. (2009)].

1.13 Magnetoelectric coupling in $BiFeO_3$

The presence of spatially modulated spiral spin structure inhibits linear magetoelectric (ME) coupling in $BiFeO_3$ but it can exhibit quadratic effect [Schmid (1994)] which is quite weak. Due to the superimposed spiral spin structure, $BiFeO_3$ does not exhibit any macroscopic magnetization and linear

magnetoelectric coupling. To observe macroscopic magnetization (i.e., M-H hysteresis loop) and linear magnetoelectric coupling, it is therefore imperative to suppress the magnetic spin spiral so that the latent magnetization due to canted spins is released. In pure $BiFeO_3$, four different ways have been proposed in the literature for the destruction of the spiral spin structure.

1.13.1 Application of the high magnetic field

Fig. 1.18(a) shows the field dependence of the longitudinal polarization in the case in which magnetic field is applied along [001] axis. At $H < H_C$ the polarization is an essentially quadratic function of the field. However, on increasing the magnetic field above $H = H_C \sim 200$ kOe, the spatially modulated spiral spin structure is destroyed and leads to a remanent magnetization as shown in Fig. 1.18(b). Above the critical field $H_C \sim 200$ kOe, the electric polarization changes sign and becomes linearly dependent on magnetic field [Popov et al (1993)]. This experiment has conclusively established that linear magnetoelectric coupling in $BiFeO_3$ can be observed by the destruction of the spatially modulated spiral spin structure leading to a homogeneous canted G-type antiferromagnetic structure. The absence of linear magnetoelectric effect in $BiFeO_3$ has been experimentally established by several other workers also [Tabares-Munoz et al. (1985); Kadomtseva et al. (2004)] for field below H_C.

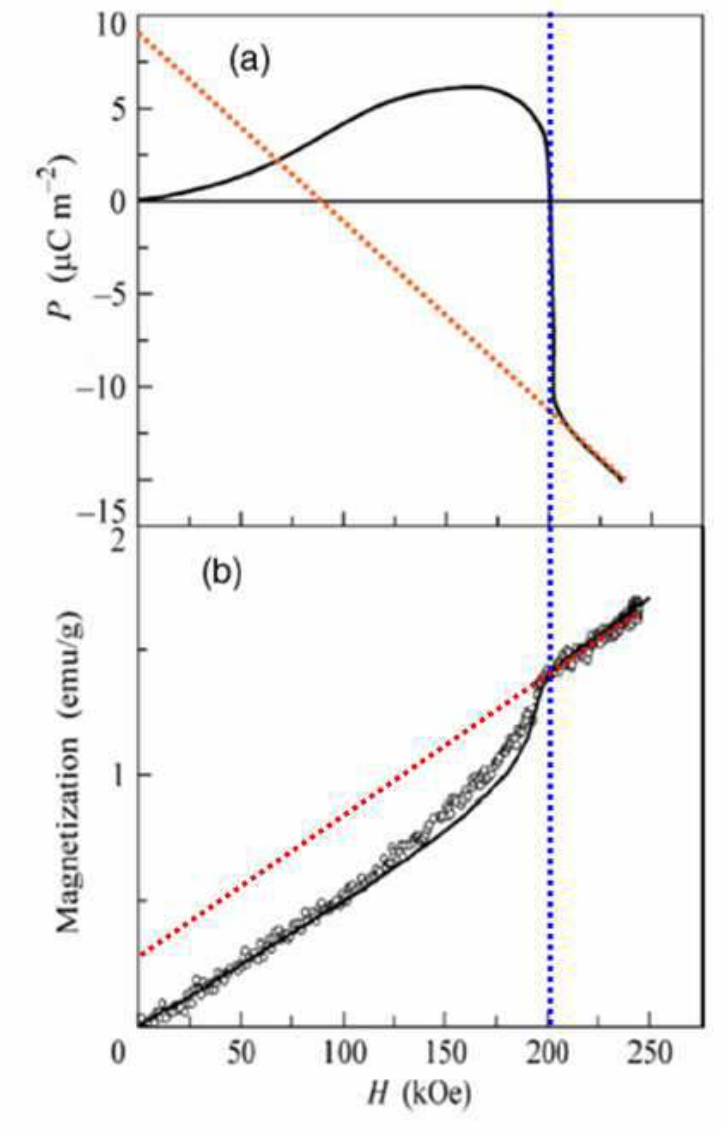

Fig.1.18 (a) Longitudinal polarization verses the strength of the magnetic field at 10 K [Popov et al. (1993)]. (b) Magnetization as a function of the amplitude of a pulsed magnetic field for H ≤ 25T for a $BiFeO_3$ at 10 K [after Catalan et al. (2009)].

1.13.2 By controlling the particle size of BF

The suppression of spiral spin structure in BF and appearance of sizable value of saturation magnetization (M_S) with the reduction of particle size of BF has been studied by different workers [Majumder et al. (2007), Park et al. (2007)].

In an early report Majumder et al. (2007) have obtained saturation magnetization value of ~ 0.40 μ_B/Fe for nanoparticles of BF in particle size range 4-40 nm, whereas in bulk form M_S is only ~ 0.024 μ_B/Fe. Park et al. (2007) have correlated strong size-dependent magnetic properties with (a) increased suppression of the spiral spin structure with decreasing nanoparticle size and (b) uncompensated spins and strain anisotropies at the surface. They have shown that the magnetic response in BF can be initiated when the particle size is less than 95 nm and it rapidly increases in the range of 270-460% for samples having particles size below 62 nm, the period length of the spiral modulated spin structure of $BiFeO_3$, as compared with that of the bulk. Hysteresis loops reported by Park et al. at room temperature for nanoparticles of BF with different particle sizes is shown in Fig.1.19. The inset shows the magnetization behavior of as–prepared $BiFeO_3$ nano-particles at 50 kOe as a function of size.

1.13.3 Thin films of BF

The spiral spin structure may also get suppressed under epitaxial constraints [Eerenstein et al. (2005)]. Saturation magnetization value of Ms ~0.06μ_B/Fe in epitaxial films of $BiFeO_3$ has been reported [Eerenstein et al. (2005)]. The magnetization values observed for $BiFeO_3$ nanoparticles and epitaxial thin films are in good agreement with the theoretically calculated value of 0.1μ_B using first principles density functional theory [Ederer et al. (2005)].

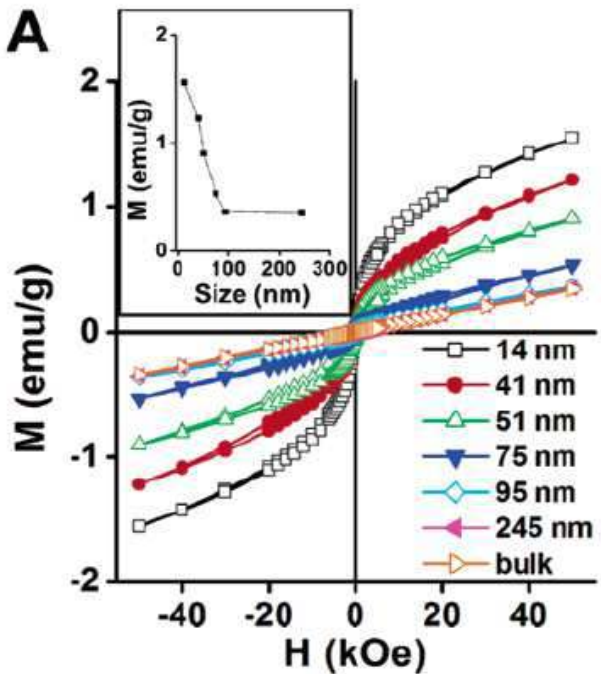

Fig. 1.19 Hysteresis loops at 300 K for $BiFeO_3$ nanoparticles with indicated sizes. The inset shows the magnetization behavior of as-prepared $BiFeO_3$ nano-particles at 50 kOe as a function of size (diameter d) [Park et al. (2007)].

1.13.4 Doping effects in BF

In recent years, attempts have been made to synthesize phase pure $BiFeO_3$ based solid solutions with a view to suppress the spiral spin structure and improve the ferroelectric properties as well by increasing the resistivities. For example, in the $BiFe_{1-x}Mn_xO_3$ system, using high resolution neutron powder diffraction (constant wavelength and time-of-flight) studies, it has been shown that the spiral spin structure of $BiFeO_3$ is modified towards homogeneous antiferromagnetic structure beyond x = 0.2 concentration (see Fig.1.20) [Sosnowska et al. (2002)]. In the $(Bi_{0.8}La_{0.2})(Fe,Ga)O_3$-45%$PbTiO_3$ system, remanent magnetizations of ~ 0.15emu/g and 0.3emu/g at T= 300 and 5 K, respectively, have been reported

[Wang et al. (2005)]. The value of remanent magnetization (M_r) observed in $(Bi_{0.8}La_{0.2})(Fe,Ga)O_3$-45%$PbTiO_3$ ceramics at low temperatures is comparable to that for pure $BiFeO_3$ at 10 K under high magnetic field. This suggests that a transition from the modulated spiral spin structure to a homogenous spin structure has occurred in the mixed system. The suppression of spiral spin structure with a non-zero remanent magnetization has been observed in several other compositionally modified $BiFeO_3$ solid solutions. Dopants like Ba^{2+}, Pb^{2+}, Sr^{2+} and Ca^{2+} at the A-site increase the radius of the *A*-site ion and lead to effective suppression of the spiral spin structure of $BiFeO_3$, resulting in the appearance of net magnetization [Khomchenko et al. (2008)]. The remanent magnetization due to suppression of spiral spin structure in $BiFeO_3$-based solids was also predicated theoretically using first principles calculations on La doped $BiFeO_3$ [Lee et al. (2010)]. Apart from the enhanced multiferroic properties when forming the solid solutions, $BiFeO_3$ exhibits different structural transformations and interesting phenomenon with increasing concentration of the alloying component [Bhattachrjee et al. (2010); Rusakov et al. (2011)]. Formation of solid solutions of $BiFeO_3$ with several other perovskite oxides with superior dielectric properties has been reported using $Pb(Fe_{1/2}Nb_{1/2})O_3$ [Kiselev et al. (1969)], $PbZrO_3$ [Ivanov et al. (2008)], $Pb(Zr_xTi_{1-x})O_3$ [Korchagina et al. (2009); Choudhary et al. (2009)], PLZT [Kanai et al. (2001)], $BaTiO_3$ [Kumar et al. (2000)], $PbTiO_3$ [Zhu et al. (2008); Bhattacharjee et al. (2010)], $BiCoO_3$ [Dieguez et al. (2011)], $NaNbO_3$ [Raevski et al. (2008)] and $BiMnO_3$ [Pálová et al. (2010)].

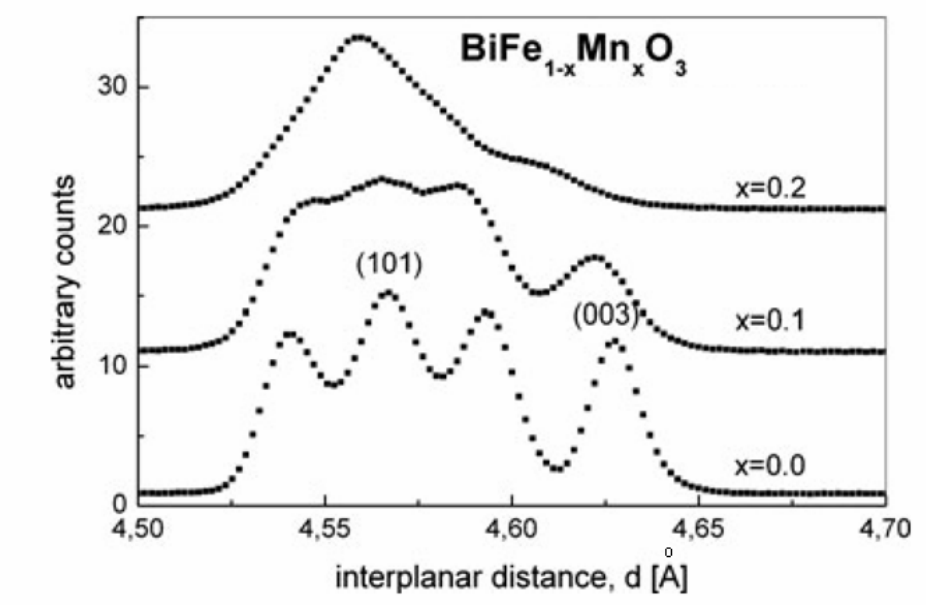

Fig.1.20 Characteristic magnetic satellite reflections for $BiMn_xFe_{1-x}O_3$ measured using OSIRIS diffractometer at ISIS [after Sosnowska et al. (2002)].

1.14 Structure and multiferroic properties of $Pb(Fe_{0.5}Nb_{0.5})O_3$

The multiferroic $Pb(Fe_{0.5}Nb_{0.5})O_3$ (PFN) belonging to the family of complex perovskites $A(B'B'')O_3$ type structure was first discovered by Smolenskii et al. [1958A]. The A-site in PFN is occupied by Pb^{2+}, while the B-site is occupied by a non-magnetic Nb^{5+} (d^0) and magnetic Fe^{3+} (d^5) ions. The d^0-ness of the Nb^{5+} cation is believed to drive the ferroelectric ordering while the presence of unpaired d electron in the Fe^{3+} (d^5) cation drives the magnetic ordering. PFN undergoes a ferroelectric to paraelectric phase transition at ~ 385 K [Plantov et al. (1970), Smolenskii et al. (1958B)]. PFN shows diffuse phase transition like relaxor ferroelectrics [Bokov and Emelyanov (1991)]. However, unlike relaxor ferroelectrics and more like normal ferroelectrics, the peak temperature T_m' is nearly frequency independent [Yasuda and Ueda (1989)]. Thus the behavior of

PFN is in between that of a normal ferroelectric and a relaxor ferroelectric [Lee et al. (2002)]. The room temperature crystal structure of the PFN is reported to be rhombohedral with R3m space group [Plantov et al. (1970), Mabud (1984), Ivanov et al. (2000)]. Some of the authors have also reported the crystal structure of the PFN at room temperature and below room temperature is monoclinic with Cm space group [Bonny et al. (1997), and Lampis et al. (1999)]. It is believed that macroscopic symmetry is likely to depend on the degree of the ordering of Fe^{3+} and Nb^{5+} ions over B-sites: B-site disorder is consistent with rhombohedral symmetry, whereas ordering of Fe^{3+} and Nb^{5+} ions would dictate a reduction of the symmetry to monoclinic.

PFN undergoes two antiferromagnetic transitions at T_{N1}~ 9 K and T_{N2}~143 K respectively [Bokov et al. (1962), Bhatt et al. (2004)]. It is believed that the paramagnetic (PM) to antiferromagnetic (AFM) transition at 143 K is related to local Fe-O-Fe antiferromagnetic superexchange, whereas the AFM to AFM transformation at ~ 9 K is related to local Fe-O-Nb-O-Fe long range chemical ordering [Schmid (1994)]. A long range G-type antiferromagnetic ordering at low temperatures has been confirmed by powder neutron diffraction studies [Pietrzak et al. (1981), Ivanov et al. (2000), Rotaru et al. (2009)]. The magnetoelectric effect in PFN was demonstrated by using the dielectric study across the magnetic transition temperature. The strong dielectric anomaly across the antiferromagnetic ordering temperature (T_N ~ 143 K) on a single crystal of PFN has been reported [Yang et al. (2004)]. The anomaly in the dielectric constant has been attributed to the magnetoelectric coupling in PFN.

1.15 Solid solutions of $BiFeO_3$ with $Pb(Fe_{1/2}Nb_{1/2})O_3$

(1-x)BF-xPFN is the solid solution of two important multiferroics $BiFeO_3$ and $Pb(Fe_{1/2}Nb_{1/2})O_3$ which show strong magnetoelectric coupling below their antiferromagnetic to paramagnetic transition temperatures ~643 K [Roginskaya et al. (1966)] and ~143 K [Bokov et al. (1962), Bhatt et al. (2004)] respectively. Therefore, BF-xPFN solid solution is interesting because possibility of changing their magnetic and ferroelectric properties with increasing doping (x). However, very little work has been carried out on this important BF-xPFN solid solution. Based on our literature survey, the research findings on this solid solution could be classified in different groups as follows;

1.15.1. Room temperature structure, dielectric and magnetic properties of BF-xPFN with composition

Many researchers have reported the room temperature crystal structure of BF-xPFN but there is no unanimity on whole phase diagram of BF-xPFN. A few important work reports about the crystal structure of BF-xPFN can be summarized as given in Table 1.2. Buhrer (1962) has reported the room temperature crystal structure of BF-xPFN for different compositions as shown in Table 1.2. The room temperature structures in the composition range $0.10 \leq x \leq 0.30$ and $0.90 \leq x \leq 1.0$ was reported to be rhombohedral (multiple-cell rhombohedral and single cell rhombohedral) while cubic in $0.80 \leq x \leq 0.40$ composition range without any specified space groups.

Table 1.2 Room temperature lattice constants of $Bi_{2x}Pb_{1-2x}Fe_{0.5+x}Nb_{0.5-x}O_3$ solid solutions with their room temperature structures for different values of x [after Buhrer (1962)].

$Bi_{2x}Pb_{1-2x}Fe_{0.5+x}Nb_{0.5-x}O_3$

x	a	α	
0.00	4.014 A	89.92°	rhombohedral
0.10	4.009	...	cubic
0.20	4.004	...	cubic
0.30	3.992	...	cubic
0.35	5.655	59.59°	rhombohedral
0.40	5.644	59.48°	rhombohedral
0.45	5.638	59.45°	rhombohedral

The lattice constant plots (rhombohedral cell parameter with respect to cubic cell and rhombohedral distortion angle) are given in Fig. 1.21. Zhdanova (1965) has reported the existence of broad morphotropic phase boundary region (MPB) for composition range $0.25 \leq x \leq 0.35$. Ismailzade and Izvestiya (1965) have reported the room temperature crystal structure of BF-0.6PFN as tetragonal in contrast to cubic as reported by Buhrer. (1962), Bhat et al. (1974) have summarized (as given in the Table 1.3) the work carried out by Krainik et al. (1965), Smolenskii and Yudin (1965), and Zhdanova (1965) and raised question about the actual crystal symmetry for the BF-0.8PFN composition. Recently, Paik et al. (2009) have also reported *P-E* loops for La substituted $(Bi_{0.9}La_{0.1})FeO_3$ -$xPb(Fe_{1/2}Nb_{1/2})O_3$ for x = 0.7 and 0.8 composition which exclude the presence of inversion symmetry for this composition.

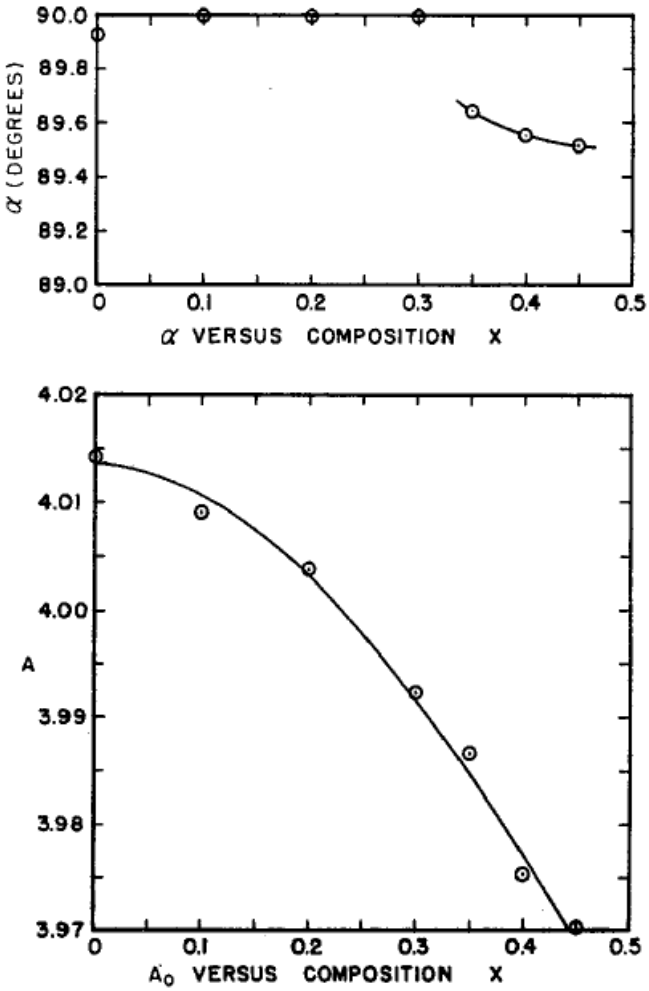

Fig. 1.21 The lattice constants plot of $Bi_{2x}Pb_{1-2x}Fe_{0.5+x}Nb_{0.5-x}O_3$ solid solutions with compositions for different values of x. The lattice constant A is plotted in terms of the pseudocubic cell parameter [after Buhrer (1962)].

Table 1.3 The lattice parameters and room temperature crystal structure of $Bi_{2x}Pb_{1-2x}Fe_{0.5+x}Nb_{0.5-x}O_3$ for different values of x [after Bhat et. al. (1974)].

Nominal composition:	$x=0$	$x=0{\cdot}1$	$x=0{\cdot}2$	$x=0{\cdot}3$
Crystal symmetry and lattice parameters:	Pseudocubic with rhombohedral distortion $a=4{\cdot}01$ Å $\alpha=89{\cdot}9°$	Pseudocubic(?) $a=4{\cdot}01$ Å	Cubic $a=4{\cdot}00$ Å	Cubic $a=3{\cdot}99$ Å

1.15.2. Ferroelectric and Magnetic Phase Transitions Studies in BF-x PFN

The ferroelectric transition temperature is determined by peak in their dielectric $\varepsilon_r^{/}(T)$ plots. Buhrer (1962) has reported the dielectric plot of $Bi_{2x}Pb_{1-2x}Fe_{0.5+x}Nb_{0.5-x}O_3$ for some selected compositions x = 0, 0.1, 0.2, 0.3 and 0.4. The dielectric peak in the $\varepsilon_r^{/}(T)$ plot at 100 kHz for x = 0.0, 0.1 and 0.3 indicate the ferroelectric to paraelectric transition for these compositions as shown in Fig.1.22. The ferroelectric transition might be occur for x = 0.3 and x = 0.4 compositions at comparatively higher temperatures.

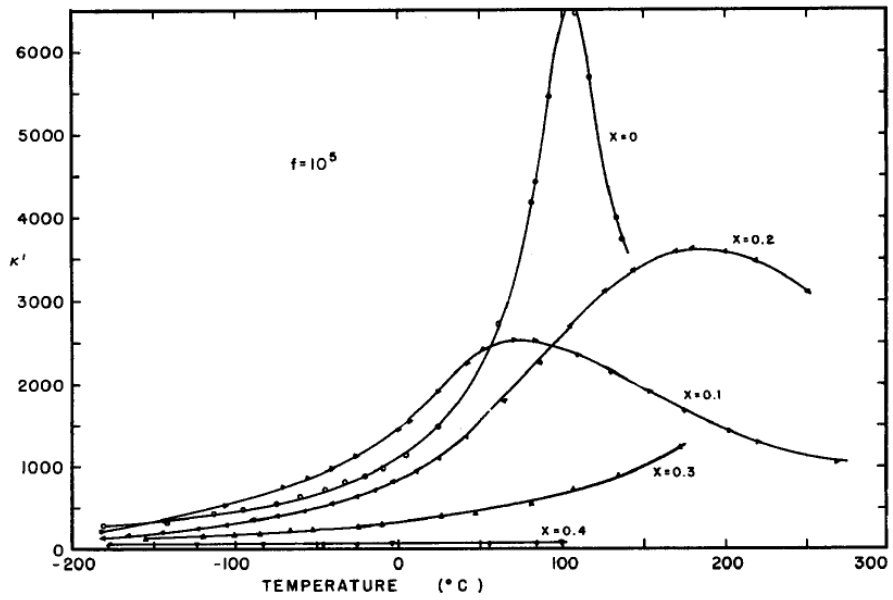

Fig.1.22 The dielectric constants ($\varepsilon_r^{/}$ or $\kappa^{/}$) of $Bi_{2x}Pb_{1-2x}Fe_{0.5+x}Nb_{0.5-x}O_3$ solid solutions for different values of x as indicated in figure at 10^5 Hz [after Buhrer (1962)].

The nature of the magnetic transition and its temperature is determined by the temperatures dependent magnetic susceptibility plot along with the *M-H* plot. The magnetic susceptibilities plots were reported for different compositions of $xBiFeO_3$-(1-x)$Pb(Fe_{1/2}Nb_{1/2})O_3$ as shown in Fig. 1.23 by Smolenskii and Yudin (1965). The typical nature of antiferroelectric to paraelectric transition was found at $BiFeO_3$ end while the weak inflexion point was observed at $Pb(Fe_{0.5}Nb_{0.5})O_3$ end. The variation of remanent magnetisation (M_r) with composition (x) was also reported by same authors as shown in Fig. 1.24.

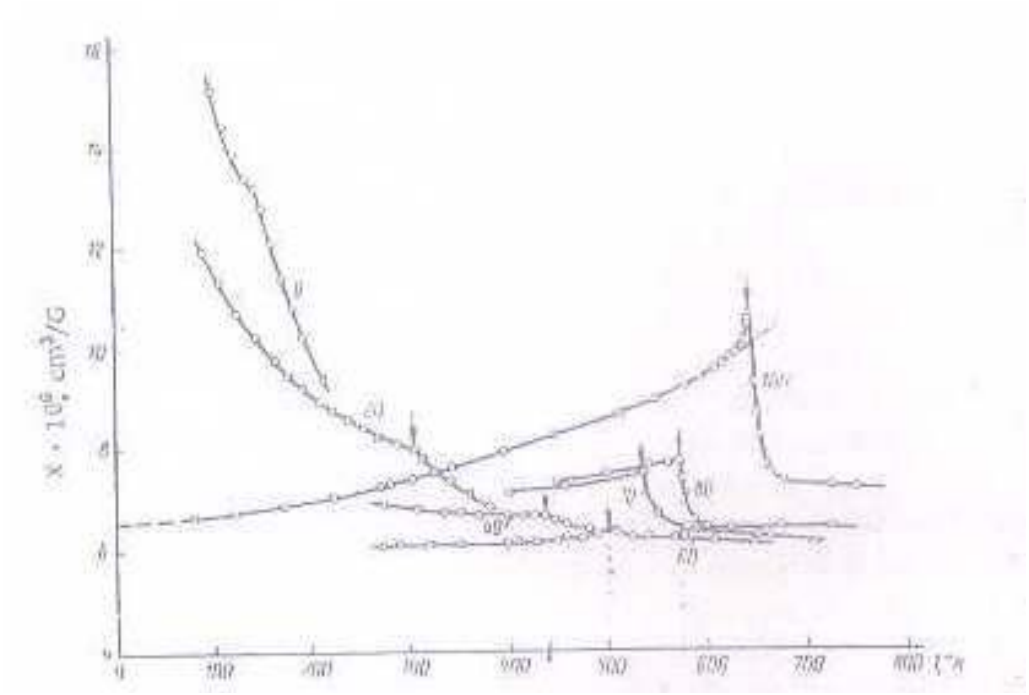

Fig.1. 23 Temperature dependences of the magnetic susceptibilities of the solid solutions (x) $BiFeO_3$-(1-x) $Pb(Fe_{0.5}Nb_{0.5})O_3$. The numbers by the curves represent the $BiFeO_3$ content in a mole percent [after Smolenskii and Yudin (1965)].

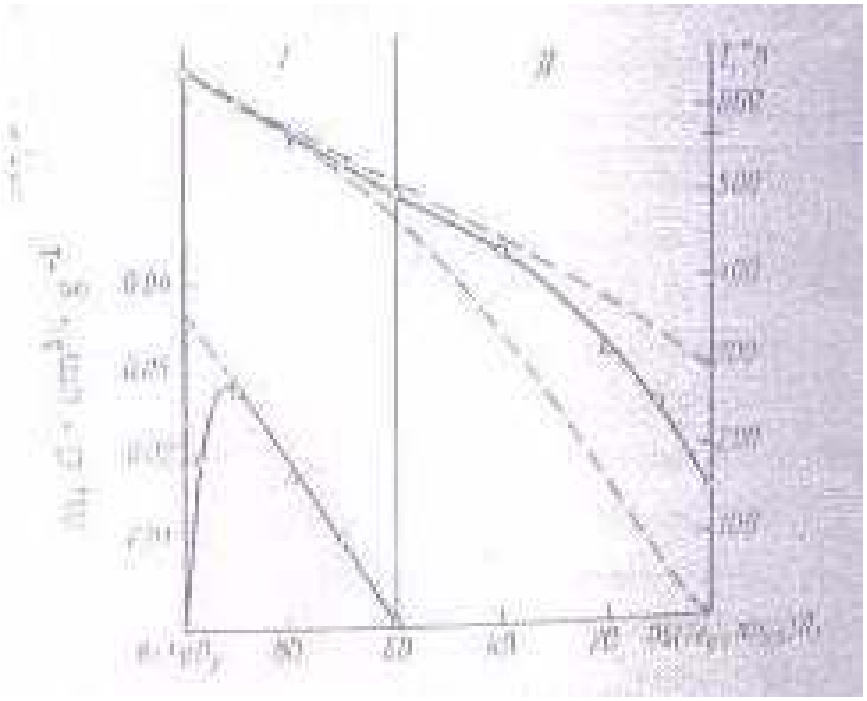

Fig. 1.24 Variation of Néel temperature (the upper continuous curve) and spontaneous magnetic moment at room temperature (the lower continuous curve) with compositions. The upper dashed curve was calculated for a random distribution of ions; the lower dashed curve was calculated for an ordered distribution of ions. I and II are regions with a complex and a simple unit cell, respectively [after Smolenskii and Yudin (1965)].

The specific heat measurement was carried by Bhat et al. of $Bi_{2x}Pb_{1-2x}Fe_{0.5+x}Nb_{0.5-x}O_3$ solid solution for x = 0.0, 0.1, 0.2 and 0.3 compositions as shown in Fig.1.25. The anomalous peaks in $Pb(Fe_{0.5}Nb_{0.5})O_3$ (x = 0) and $Bi_{0.2}Pb_{0.8}(Fe_{0.6}Nb_{0.4})O_3$ (x = 0.1) have been correlated with their ferroelectric Curie points, and those in $Bi_{0.4}Pb_{0.6}(Fe_{0.7}Nb_{0.3})O_3$ (x = 0.2) and $Bi_{0.6}Pb_{0.4}(Fe_{0.8}Nb_{0.2})O_3$ (x = 0.3) with their Néel points. The ferroelectric T_C and antiferromagnetic T_N were also given in

Table 1.4 for different compositions of $Bi_{2x}Pb_{1-2x}Fe_{0.5+x}Nb_{0.5-x}O_3$ obtained by dielectric, magnetic and specific measurements by different researchers.

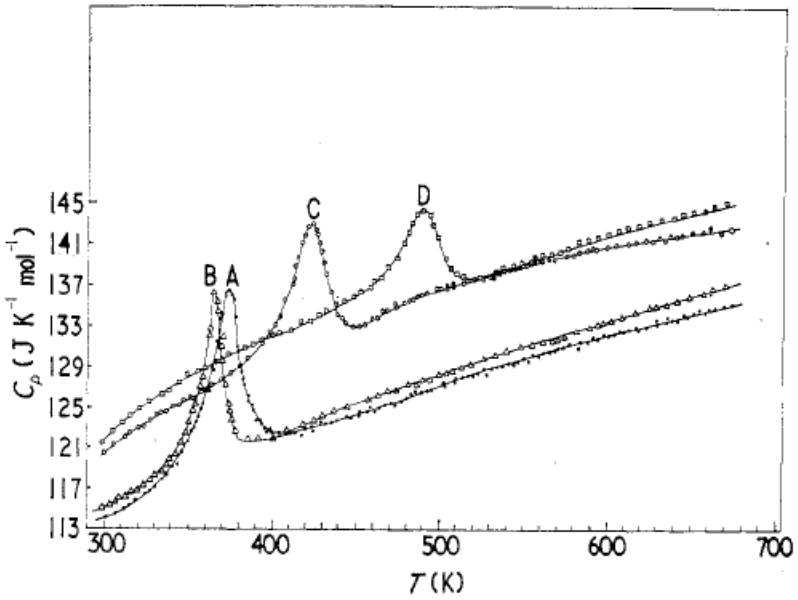

Fig.1.25 Temperature variation of heat capacity of $Bi_{2x}Pb_{1-2x}Fe_{0.5+x}Nb_{0.5-x}O_3$ solid solutions system. The curves A, B, C and D for x = 0.0, 0.1, 0.2 and 0.3 respectively.

Table 1.4 The magnetic and ferroelectric transitions temperatures determined by dc magnetic susceptibility, dielectric constant and specific heat measurements of $Bi_{2x}Pb_{1-2x}Fe_{0.5+x}Nb_{0.5-x}O_3$ for different values of x [after Bhat et. al. [1974)].

Nominal composition:	$x=0$	$x=0{\cdot}1$	$x=0{\cdot}2$	$x=0{\cdot}3$
Transition temperature (K)				
χ studies:	143	300	425	510
Dielectric studies:	383	353	453	—
Present work:				
Calorimetric studies:	374 ± 1	365 ± 1	424 ± 1	492 ± 1

1.16 Objectives of the present work

The main objectives of the present work on the BF-xPFN solid solutions are as follows:

1. To synthesize pure phase solid solution of (1-x)$BiFeO_3$-x$Pb(Fe_{0.5}Nb_{0.5})O_3$.

2. To study the room temperature crystal structure of (1-x)$BiFeO_3$-x $Pb(Fe_{0.5}Nb_{0.5})O_3$ solid solution over the entire composition range.

3. To study the nature of ferroelectric to paraelectric phase transition in multiferroic $BiFeO_3$-0.2$Pb(Fe_{0.5}Nb_{0.5})O_3$ solid solution.

4. To study the effect of $Pb(Fe_{0.5}Nb_{0.5})O_3$ substitution on the magnetic structure and magnetic properties of $BiFeO_3$ over the entire composition range.

5. To understand the origin of magnetoelectric coupling at the atomic level in $BiFeO_3$-0.2$Pb(Fe_{0.5}Nb_{0.5})O_3$ solid solution.

6. The composition and temperature dependent dielectric study of (1-x)$BiFeO_3$-x$Pb(Fe_{0.5}Nb_{0.5})O_3$ solid solutions.

7. To establish a structural and magnetic phase diagram of (1-x)$BiFeO_3$-x$Pb(Fe_{0.5}Nb_{0.5})O_3$ solid solution.

The results of the present investigations are described in the subsequent chapters of this thesis.